ISTITUTO NAZIONALE DI RICERCA METROLOGICA
Repository Istituzionale

Quantum Critical Behavior of One-Dimensional Soft Bosons in the Continuum

(Article begins on next page)

05 December 2024

Quantum Critical Behavior of One-Dimensional Soft Bosons in the Continuum

Stefano Rossotti,[1] Martina Teruzzi,[2,1] Davide Pini,[1] Davide Emilio Galli,[1] and Gianluca Bertaina[1,∗]

[1]*Dipartimento di Fisica, Università degli Studi di Milano, via Celoria 16, I-20133 Milano, Italy*
[2]*International School for Advanced Studies (SISSA), Via Bonomea 265, Trieste, Italy*

We consider a zero-temperature one-dimensional system of bosons interacting via the soft-shoulder potential in the continuum, typical of dressed Rydberg gases. We employ quantum Monte Carlo simulations, which allow for the exact calculation of imaginary-time correlations, and a stochastic analytic continuation method, to extract the dynamical structure factor. At finite densities, in the weakly-interacting homogeneous regime, a rotonic spectrum marks the tendency to clustering. With strong interactions, we indeed observe cluster liquid phases emerging, characterized by the spectrum of a composite harmonic chain. Luttinger theory has to be adapted by changing the reference lattice density field. In both the liquid and cluster liquid phases, we find convincing evidence of a secondary mode, which becomes gapless only at the transition. In that region, we also measure the central charge and observe its increase towards $c = 3/2$, as recently evaluated in a related extended Bose-Hubbard model, and we note a fast reduction of the Luttinger parameter. For 2-particle clusters, we then interpret such observations in terms of the compresence of a Luttinger liquid and a critical transverse Ising model, related to the instability of the reference lattice density field towards coalescence of sites, typical of potentials which are flat at short distances. Even in the absence of a true lattice, we are able to evaluate the spatial correlation function of a suitable pseudo-spin operator, which manifests ferromagnetic order in the cluster liquid phase, exponential decay in the liquid phase, and algebraic order at criticality.

Quantum phase transitions (QPT) [1] play an intriguing role in many-body systems, due to the possibility of unveiling new exotic phases. Thanks to the progress achieved in the manipulation of ultracold gases with magneto-optical traps, it is possible to explore the physics related to QPTs by engineering well-controlled synthetic quantum many-body systems, confined for example by optical lattices [2, 3] or in quasi-one-dimensional geometries [4–7]. Recently, Rydberg atoms [8] have emerged as a new route to QPTs [9, 10]. These are atoms in highly-excited electronic states, so that their electronic cloud is very large. In particular, theoretical [11–14] and experimental [15–17] efforts have been put in the study of ensembles of *dressed* Rydberg atoms, which are superpositions of the ground state and the above mentioned excited state, coupled via a Rabi process. Their effective interaction can be a soft-shoulder potential, with a flat repulsion up to a radius R_c related to the highly excited state, and a repulsive van-der-Waals tail at large distances [11, 12, 18–21]. Interestingly, for this class of interactions, quantum cluster phases have been predicted in the high-density and interaction strength regime, yielding supersolid behavior in high dimensions [11–13, 22] and cluster Luttinger liquids (CLL) in one dimension (1D) on a lattice [23, 24].

In this Letter, we investigate a prototypical system of N bosons in 1D at linear particle density n, governed by the following Hamiltonian in the continuum:

$$H = -\frac{\hbar^2}{2m} \sum_i^N \frac{\partial^2}{\partial x_i^2} + \sum_{i<j} \frac{V_0}{r_{ij}^6 + R_c^6} \qquad (1)$$

where x_i are the particle coordinates, $r_{ij} = |x_i - x_j|$ the distances, m is the mass and V_0 and R_c are the strength and the radius of the soft-shoulder interaction potential $V(r)$. If not otherwise specified, in the following we use units of R_c for the length, $E_c = \hbar^2/mR_c^2$ for the energy, and $\hbar/R_c$ for the momenta (See Supplemental Material [25]). The zero-

temperature phase diagram (Fig. 1) thus depends on the following two dimensionless quantities: strength, $U = V_0/(E_c R_c^6)$, and density, $\rho = nR_c$. By evaluating relevant static and dynamical properties, we will show that, while for small U and moderate ρ the system is a Luttinger liquid (LL) [26], although with strong correlation effects, for higher U or ρ a transition occurs towards CLL. In particular, we will focus on the QPT to the dimer cluster liquid, which turns out to be of the 2D Ising universality class. A similar phenomenology has been recently studied in a 1D lattice system governed by the extended Bose-Hubbard hamiltonian [23, 24], while we observe it for the first time in the continuum, where we find that an effective spin hamiltonian emerges at the transition, *even in absence of an underlying lattice*.

For generic coupling and density, this system falls into the LL universality class [26], characterized by a gapless bosonic mode at small momenta, with sound velocity v. The low-energy and momentum sector of the Hilbert space is governed
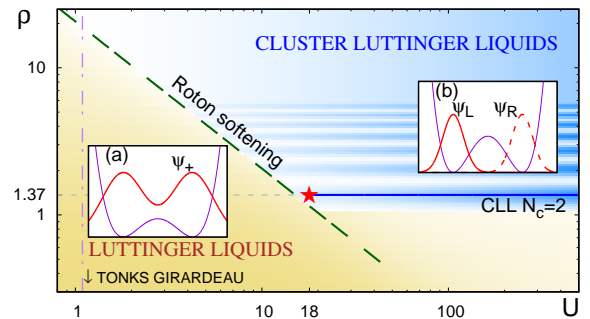

FIG. 1. Phase diagram (log-log scale). A star marks the critical point between the LL and CLL phases for densities commensurate to 2-particle clusters. The long-dashed line corresponds to the softening of the Bogoliubov roton. (a) Delocalized orbital in the effective double-well. (b) Localized left and right orbitals.
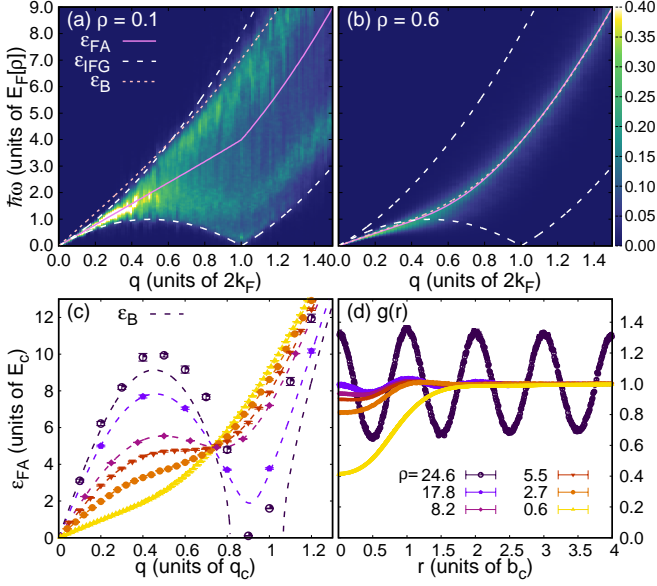
FIG. 2. Dynamical structure factor at $U = 1.09$, as a function of momentum q and energy transfer $\varepsilon = \hbar\omega$. Magnitude (color box) is in units of $1/E_F$ (values beyond scale are plotted in white). Liquid phase at low (a) and intermediate ρ (b). (c) Evolution of Feynman approximation, compared to Bogoliubov approximation. (d) Pair distribution function.

by the Hamiltonian $H_{LL} = (v/2\pi) \int dx [K_L(\nabla\theta)^2 + (\nabla\phi)^2/K_L]$, where a large Luttinger parameter $K_L > 1$ favors the fluctuation of the particle counting field $\phi(x)$, while small values of K_L induce crystal-like behavior, by disordering the phase field $\theta(x)$. The central charge of the associated conformal field theory (CFT) is $c = 1$ [27] and, for our Galilean invariant system, $v = \rho\pi/K_L$ [26].

In the dilute limit, the effects of the interaction are well described by the scattering length a_{1D}; in particular, for $U \sim 1.09$, we get $a_{1D} \sim 0$ [28], corresponding to the Tonks–Girardeau (TG) model [29]. Conversely, at higher densities, the full shape of $V(r)$ is relevant. Its 1D Fourier transform $\tilde{V}$ [25] features a global minimum at $q_c \simeq 4.3$, at which $\tilde{V}(q_c) < 0$, providing a typical length $b_c = 2\pi/q_c \simeq 1.46$. It has been recognized, in the context of classical physics, that such preferred distance, independent of density, favors clustering, even if the potential is completely repulsive [30, 31]. Classically, at $T = 0$, one obtains a cluster crystal, which is destabilized in 1D by finite temperature, in favor of cluster-dominated liquid phases with different average occupation [32, 33]. Quantum mechanics provides a source of *coherent* delocalization even at $T = 0$, which renders the cluster phase a CLL and can trigger a QPT towards a LL without cluster order (Fig. 1).

To study the phase diagram in a non-perturbative way, we use the well-established path integral ground state (PIGS) quantum Monte Carlo method [34, 35], which represents the ground state as the imaginary-time projection $\exp(-\tau H)|\Psi_T\rangle$ of a trial wavefunction. We simulate up to $N = 200$ particles in a segment of length $L = N/\rho$, using periodic boundary con-

ditions (PBC). The trial wavefunction is of the two-body Jastrow form: $\Psi_T(x_1 \ldots x_N) = \exp\left[-\frac{1}{2}\sum_{i<j}\left(u(r_{ij}) + \chi(r_{ij})\right)\right]$, where $\chi(r)$ accounts for long-wavelength phonons [28, 36], while $\exp[-u(r)/2]$ is the numerical solution of a suitable two-body Schrödinger equation [28], with the effective potential $V_{eff}(r) = c_1 V(r) + c_2 \sum_l V(r - lb)$. To reduce projection times, it is crucial to use and optimize this mean-field potential, which accounts for the presence of nearby clusters [25]. We consider excitations associated to density fluctuations, which are commonly investigated via the dynamical structure factor $S(q,\omega) = \int dt \frac{e^{i\omega t}}{2\pi N} \langle e^{itH/\hbar}\rho_q e^{-itH/\hbar}\rho_{-q}\rangle$. The PIGS algorithm evaluates the numerically exact imaginary-time intermediate scattering function, which yields $S(q,\omega)$ via analytic continuation through the genetic inversion via falsification of theories algorithm [25, 37–40].

We now proceed to discuss our results, first in the LL, then in the CLL regimes. Finally, we discuss the QPT in between the two liquids.

Liquid regime– We concentrate on interaction $U \simeq 1.09$, and increase the density (dot-dashed line in Fig. 1). In the low-density regime $\rho \lesssim 0.1$ (Fig. 2a), $S(q,\omega)$ is almost flat in between the particle-hole boundaries $\varepsilon_{IFG}(q) = |k_F q \pm q^2/2|$, analogously to the TG gas, which can be mapped to an ideal Fermi gas (IFG). Here and in the following, $k_F = \pi\rho$ and $E_F = k_F^2/2$ are effective Fermi momentum and energy. We note that, already at $\rho = 0.6$ (panel b), the system becomes relatively more compressible, due to the soft-core interaction. It is manifest that, for $\rho \gtrsim 0.6$, the spectrum is peaked along a main mode, which is very well described by Feynman approximation $\varepsilon_{FA}(q) = \varepsilon_0(q)/S(q)$, with $\varepsilon_0(q) = q^2/2$ the free-particle energy and $S(q)$ the static structure factor [41]. By further increasing the density, the main excitation becomes more structured, with a roton minimum that moves towards $q = q_c$ (Fig. 2c). A standard Bogoliubov analysis [11, 20] yields the dispersion $\varepsilon_B(q) = \sqrt{\varepsilon_0(q)\left[\varepsilon_0(q) + 2\rho\tilde{V}(q)\right]}$, which depends only on the combination $\alpha = \rho U$. In this approximation, it is clear that the emergence of the roton minimum is allowed by the introduction of the momentum dependence of $\tilde{V}$, which has a negative part [42, 43]. The roton softens at $\alpha = \alpha_c \simeq 20.65$. While the agreement between $\varepsilon_{FA}(q)$ and $\varepsilon_B(q)$ is very good for $\rho \lesssim 19$, Bogoliubov treatment is in general not valid anymore for $U \gtrsim \alpha_c/\rho$, where indeed our simulations show that clustering occurs (dashed line in Fig. 1). Another interesting observation is that at $q_0 \simeq 3.143$, the first zero of $\tilde{V}$, one has $\varepsilon_B(q_0) = \varepsilon_0(q_0)$, independently of ρ and U (Fig. 2c). This universal point in the excitation spectrum is present whenever Bogoliubov approximation is valid and $\tilde{V}(q_0) = 0$.

On increasing ρ, the pair distribution function $g(r)$ at first gradually approaches 1 everywhere (Fig. 2d), as in classical soft-core fluids in the absence of clustering [44]. However, for very high ρ, large-amplitude slowly-decaying oscillations appear, with wavelength b_c. Again, this behavior is akin to that of classical systems, in the presence of clustering [30]. A gaussian fit of the peaks indicates the average presence of $N_c \simeq 36$ particles per cluster at $\rho = 24.6$. In the quantum
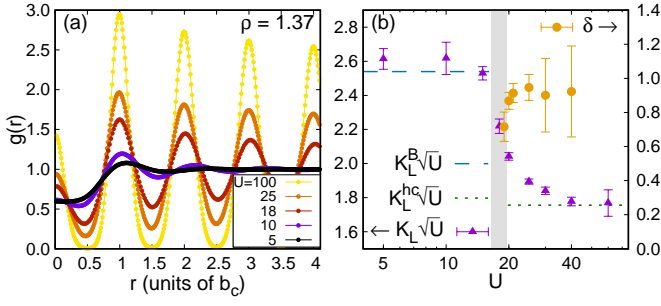
FIG. 3. (a) Pair distribution function at $\rho = 1.37$ from the LL to the CLL phases. (b) Left y-axis: Luttinger parameter (scaled by $\sqrt{U}$) in linear-log scale (triangles), compared to Bogoliubov $K_L^B = \sqrt{3\pi\rho/2U}$, and harmonic chain $K_L^{hc} = [\pi/\varepsilon_h(b_c)](\rho/b_c^3)^{1/2}$ predictions. Right y-axis: excess particles per cluster δ (circles). A band highlights the transition region.

case, the oscillations of $g(r)$ eventually decay as in a cluster liquid, a behavior that we can easily see in the more relevant cluster phases at low ρ and large U. In fact, a hamiltonian description of dressed Rydberg gases is questionable at high ρ, due to increased losses to other Rydberg levels in current experiments [25].

Commensurate Cluster Luttinger Liquid– We therefore now focus on the density $\rho = 2/b_c \simeq 1.37$ (solid line in Fig. 1), commensurate to clusters made of $N_c = 2$ particles [45]. In Fig. 3a, the PIGS results for $g(r)$ are shown, indicating an evolution to a cluster structure on increasing U, where the peaks are consistent with Gaussians containing two particles. $g(r)$ manifests long-range algebraic decay of the peaks' heights, which demonstrates absence of true crystal order [46]. To interpret these results, we model this regime with CLL theory. In the standard bosonization approach [26], the counting field measures fluctuations around a lattice with spacing ρ^{-1}: hamiltonian H_{LL} is then derived with the assumption that fluctuations are small. However, in a commensurate cluster liquid, clearly fluctuations are small only around a lattice of clusters, with spacing $\rho^{-1}N_c = b_c$. We follow [23, 24], and obtain the following commensurate CLL form of $g(r)$:

$$g(r) \underset{r\gg 1/\rho}{\simeq} 1 - \frac{2K_L}{(2\pi\rho r)^2} + \sum_{l=1}^{\infty} A_l \frac{\cos(2\pi l\rho r/N_c)}{r^{2K_L'l^2}} \quad (2)$$

The r^{-2} term is analog to the standard LL case, while the dominant contribution in the last term yields density oscillations of wavevector $2k_F/N_c = q_c$, modulated by an effective Luttinger parameter $K_L' = K_L/N_c^2$. This implies that, in the CLL phase, the divergence of $S(q_c) \propto N^{1-2K_L'}$ is much stronger than what would result from K_L. We extract K_L and K_L' from the small momentum behavior of $S(q)$ and large distance decay of $g(r)$, respectively [25]. Interestingly, K_L scales as $U^{-1/2}$ in both the LL and CLL regimes, but with different prefactors. Moreover, we verify that the number of excess particles per cluster $\delta = \sqrt{K_L/K_L'} - 1$ quickly goes to 1 for $U > 18$ (Fig. 3b).

Deeply in the cluster phase, a composite harmonic chain (HC) theory can also be envisaged. We write a model hamil-

tonian of the type $H_{hc} = \sum_{iv} p_{i,v}^2/2 + \gamma \sum_{iv\mu}(x_{i,v} - x_{i+1,\mu})^2/2$, where $x_{i,v}$ is the displacement of the v-th particle (with $1 \le v \le N_c$) from the average position of cluster i (with $1 \le i \le N/N_c$), and harmonic springs of strength γ are present only between particles in adjacent clusters, modeling the fact that $V(r)$ is flat at short distances [47]. We obtain center-of-mass modes, of acoustic frequencies $\varepsilon_{HCA}(k) = 2\sqrt{N_c}\varepsilon_h \sin(kb_c/2)$, being $\varepsilon_h = \sqrt{\gamma}$, and optical modes, of dispersionless frequency $\varepsilon_{HCO} = \sqrt{2N_c}\varepsilon_h$. The latter correspond to vibrations of the relative distances of particles in a cluster. We relate ε_h to the mean-field potential felt by a particle if all the others are in a cluster crystal with spacing b, and find $\varepsilon_h(b) = \sqrt{-(4\pi^2/b^3)\sum_{j=1}^{\infty} j^2\tilde{V}(2\pi j/b)}$ [48]. It is clear that a stable structure is possible only if $\tilde{V}(2\pi/b) < 0$ for some b [31, 49].

In Fig. 4e, the spectrum at $U = 100$ is shown: the main peak is in good agreement with the acoustic mode of HC theory, with $b = b_c$. A secondary structure appears at higher frequencies, which we interpret as the HC optical mode [13]. This is however not flat, but strongly modified by anharmonic couplings: these are clearly even more crucial at smaller U, where they induce cluster melting.

Ising transition– The question is now: how are the LL and CLL phases really different? Is the transition simply a crossover? Our data, which show Luttinger liquid behavior on both sides, exclude a Berezinskii-Kosterlitz-Thouless transition to a charge-density-wave, or Peierls dimerization transition, even though, at $U = 18$, we get $K_L \simeq 0.52(1)$ [27]. Moreover, the atomic-pair superfluid transition [50] is also excluded, since, here, formation of larger clusters is allowed and the CLL phase is characterized by strong quasi-solid order ($K_L < 1/2$).

In fact, the physics of this relatively simple system turns out to be very rich, as can be seen in the spectra across the transition (Fig. 4). The main rotonic mode gradually softens at $q \simeq q_c$ (panels a-b), which, at this density, corresponds to k_F. After the transition, to be located at $U = U_c \simeq 18$ (panel c), this lowest mode starts to match the HC acoustic mode (panels d-e), which is gapless at $q = q_c$. Quite interestingly, a weaker secondary mode appears not only in the cluster phase, but also in the strongly correlated liquid phase, in the form of a *secondary roton*, which connects to the higher-momenta main mode, as in an avoided crossing. It is reasonable to associate this secondary excitation, in the LL phase, to incipient cluster formation, due to particles being preferentially localized close to either the left or the right neighbor. The crucial observation is that the gap of both such LL excitations (panels a-b), and the anharmonic optical modes of the CLL phase (d-e), vanishes at the transition (c), which implies that they proliferate at that point. This behavior is consistent with that of the 1D transverse Ising (TI) model [51–55] of a chain of coupled two-level systems. Its hamiltonian is $H_{TI} = -J\sum_i \sigma_i^z\sigma_{i+1}^z - h\sum_i \sigma_i^x$, where $\sigma_i^{x/z}$ are Pauli matrices at site i. It contains both a ferromagnetic coupling ($J > 0$), which forces alignment, and quantum tunneling ($h > 0$) between the eigenstates of σ^z, which
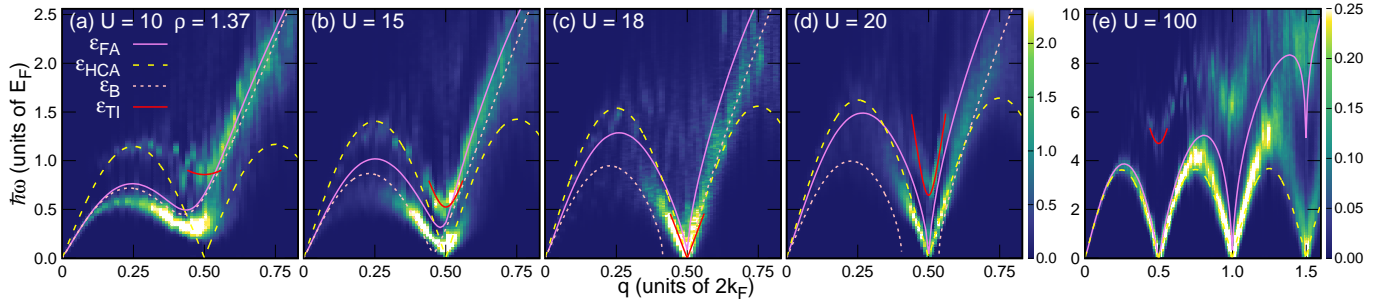
FIG. 4. Spectra at $\rho = 1.37$ along the transition, compared to Feynman ε_{FA} and Bogoliubov ε_B approximations, and the harmonic chain acoustic mode ε_{HCA}. At $q \simeq q_c$, the secondary mode is fitted by the Ising spectrum ε_{TI}. Panel e has different ranges. Color scale as in Fig. 2a.

favors a paramagnetic state. This model is exactly solvable with a Jordan-Wigner transformation and Bogoliubov diagonalization [56] and yields excitations of energy

$$\varepsilon_{TI}(q) = \sqrt{\Delta^2 + 4Jh\left(\sin qa/2\right)^2} \, , \qquad (3)$$

where $\Delta = |J - h|$ is the gap and a is lattice spacing, which are gapless only for $h = J$. This signals a QPT from the ferromagnetic to the paramagnetic state, which is dual to the 2D classical thermal Ising transition. In our case, it is natural to associate Δ to the gap of the secondary mode at $q = q_c$, and set $a = b_c$, implying that a spin should be identified every two particles. We fit Eq. (3) from our spectral functions (Fig. 5a): within our accuracy, the behavior of Δ in $U - U_c$ is linear close to the transition, consistent with the dynamical exponent $z = 1$. The point at $U = 18$ requires very long projection times: another indication of the presence of a very low-energy mode. Within our resolution, the Luttinger and critical Ising modes have the same velocity at $U = U_c$, which would imply low-energy supersymmetry [57].

To corroborate our interpretation, we recall that the central charge c of the critical TI model is $c = 1/2$, so that, at the transition, the total central charge should be $c = 1 + 1/2 = 3/2$, as calculated for the related lattice model [24]. We estimate c from the slope of the energy per particle $\varepsilon(N) = \varepsilon_\infty - cE_F/(6K_LN^2)$ versus $1/N^2$, employing a standard CFT result

for the dominant finite-size effects [58, 59]. An increase of c is manifest in Fig. 5a. It is in fact delicate to extrapolate c close to U_c: higher order corrections may become relevant, and field theoretical methods should elucidate the interplay between the Luttinger and Ising fields, as done in [57, 60].

It is particularly appealing to investigate the microscopic realization of this effective TI model. The many-body potential surface reduces to double wells as a function of relative distances: two nearby bosons have preferred configurations if they are at $r_{ij} = 0$ or $r_{ij} \simeq b_c$ [25]. Thus, for each even particle, for example, there are left ψ_L and right ψ_R preferred cluster configurations, and the potential energy is minimized when subsequent even particles choose the same direction for clustering. Anharmonic terms give instead rise to delocalization. The cluster phase is then to be thought as the ferromagnetic state where all even particles have chosen either ψ_L or ψ_R (Fig. 1b), while the liquid phase is made of $\psi_+ = (\psi_L + \psi_R)/\sqrt{2}$ states (Fig. 1a), where particles continuously hop left and right.

This mapping can be made quantitative, by introducing a simple, but effective *string* representation of σ^z, inspired by [54]: first, particles are *ordered by their position k*, and even positions are assigned a lattice index $i = k/2$; then, a pseudo-spin $\sigma_i^z = 1$ is assigned if $|x_k - x_{k-1}| < |x_k - x_{k+1}|$, or $\sigma_i^z = -1$ in the opposite case. A spatial correlator of this $\mathbb{Z}_2$ pseudo-spin can be evaluated as $g_\sigma(|i - j|) = \langle \sigma_i^z \sigma_j^z \rangle$ (Fig. 5b). It is very remarkable that g_σ behaves as expected for the TI model: in the LL (paramagnetic) phase it decays exponentially, while in the CLL (ferromagnetic) phase it manifests true long-range order, which is *nonlocal* [54, 61, 62], because of the preliminary ordering of particles. At $U = 18$, its behavior is close to an algebraic decay with exponent $\eta \simeq -1/4$.

This pseudo-spin mapping in a continuous system at the LL-CLL transition, as revealed by excitation spectra and a suitable spin correlator, is the key result of this Letter. Such critical regime could be probed even at finite T, given the finite size of experiments. Future work will investigate effects of non commensurability of ρ with $1/b_c$, which is particularly relevant for trapped gases.
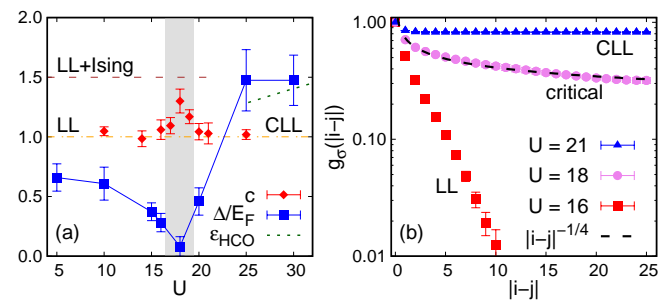
FIG. 5. (a) Second mode gap Δ (squares), compared to the optical mode energy ε_{HCO} (dotted line); central charge c (diamonds). (b) Log-linear scale: pseudo-spin correlators, compared to the critical behavior (dashed line).

---

* gianluca.bertaina@unimi.it

[1] S. Sachdev, *Quantum Phase Transitions* (Cambridge University Press, Cambridge, 2000).

[2] J. Simon, W. S. Bakr, R. Ma, M. E. Tai, P. M. Preiss, and M. Greiner, Nature **472**, 307 (2011).

[3] X. Zhang, C.-L. Hung, S.-K. Tung, and C. Chin, Science **335**, 1070 (2012).

[4] M. A. Cazalilla, R. Citro, T. Giamarchi, E. Orignac, and M. Rigol, Rev. Mod. Phys. **83**, 1405 (2011).

[5] M. Olshanii, Phys. Rev. Lett. **81**, 938 (1998).

[6] E. Haller, M. Gustavsson, M. J. Mark, J. G. Danzl, R. Hart, G. Pupillo, and H.-C. Nägerl, Science **325**, 1224 (2009).

[7] E. Haller, R. Hart, M. J. Mark, J. G. Danzl, L. Reichsöllner, M. Gustavsson, M. Dalmonte, G. Pupillo, and H.-C. Nägerl, Nature **466**, 597 (2010).

[8] R. Löw, H. Weimer, J. Nipper, J. B. Balewski, B. Butscher, H. P. Büchler, and T. Pfau, J. Phys. B: At. Mol. Opt. Phys. **45**, 113001 (2012).

[9] H. Weimer, R. Löw, T. Pfau, and H. P. Büchler, Phys. Rev. Lett. **101**, 250601 (2008).

[10] P. Schauß, M. Cheneau, M. Endres, T. Fukuhara, S. Hild, A. Omran, T. Pohl, C. Gross, S. Kuhr, and I. Bloch, Nature **491**, 87 (2012).

[11] N. Henkel, R. Nath, and T. Pohl, Phys. Rev. Lett. **104**, 195302 (2010).

[12] F. Cinti, T. Macrì, W. Lechner, G. Pupillo, and T. Pohl, Nat. Commun. **5**, 3235 (2014).

[13] As also suggested in the 2D case in S. Saccani, S. Moroni, and M. Boninsegni, Phys. Rev. Lett. **108**, 175301 (2012).

[14] A. Lauer, D. Muth, and M. Fleischhauer, New J. Phys. **14**, 095009 (2012).

[15] Y.-Y. Jau, A. M. Hankin, T. Keating, I. H. Deutsch, and G. W. Biedermann, Nat Phys **12**, 71 (2016).

[16] J. Zeiher, R. van Bijnen, P. Schauß, S. Hild, J.-Y. Choi, T. Pohl, I. Bloch, and C. Gross, Nat. Phys. **12**, 1095 (2016).

[17] J. Zeiher, J.-Y. Choi, A. Rubio-Abadal, T. Pohl, R. van Bijnen, I. Bloch, and C. Gross, arXiv:1705.08372 (2017).

[18] G. Pupillo, A. Micheli, M. Boninsegni, I. Lesanovsky, and P. Zoller, Phys. Rev. Lett. **104**, 223002 (2010).

[19] J. B. Balewski, A. T. Krupp, A. Gaj, S. Hofferberth, R. Löw, and T. Pfau, New J. Phys. **16**, 063012 (2014).

[20] T. Macrì, S. Saccani, and F. Cinti, J. Low Temp. Phys. **177**, 59 (2014).

[21] M. Płodzień, G. Lochead, J. de Hond, N. J. van Druten, and S. Kokkelmans, Phys. Rev. A **95**, 043606 (2017).

[22] F. Ancilotto, M. Rossi, and F. Toigo, Phys. Rev. A **88**, 033618 (2013).

[23] M. Mattioli, M. Dalmonte, W. Lechner, and G. Pupillo, Phys. Rev. Lett. **111**, 165302 (2013).

[24] M. Dalmonte, W. Lechner, Z. Cai, M. Mattioli, A. M. Läuchli, and G. Pupillo, Phys. Rev. B **92**, 045106 (2015).

[25] See Supplemental Material at [URL will be inserted by publisher] for details on the potential, the experimental realization, the methods, the extraction of relevant observables.

[26] F. D. M. Haldane, Phys. Rev. Lett. **47**, 1840 (1981).

[27] T. Giamarchi, *Quantum Physics in One Dimension* (Oxford University Press, 2003).

[28] M. Teruzzi, D. E. Galli, and G. Bertaina, J. Low Temp. Phys. **187**, 719 (2017). Recall that the definition of the scattering length in 1D implies that it is zero for infinite zero-range repulsion.

[29] M. Girardeau, J. Math. Phys. **1**, 516 (1960).

[30] C. N. Likos, A. Lang, M. Watzlawek, and H. Löwen, Phys. Rev. E **63**, 031206 (2001).

[31] B. M. Mladek, D. Gottwald, G. Kahl, M. Neumann, and C. N. Likos, Phys. Rev. Lett. **96**, 045701 (2006).

[32] S. Prestipino, Phys. Rev. E **90**, 042306 (2014).

[33] S. Prestipino, D. Gazzillo, and N. Tasinato, Phys. Rev. E **92**, 022138 (2015).

[34] A. Sarsa, K. E. Schmidt, and W. R. Magro, J. Chem. Phys. **113**, 1366 (2000).

[35] M. Rossi, M. Nava, L. Reatto, and D. E. Galli, J. Chem. Phys. **131**, 154108 (2009).

[36] L. Reatto and G. Chester, Phys. Rev. **155**, 88 (1967).

[37] E. Vitali, M. Rossi, L. Reatto, and D. E. Galli, Phys. Rev. B **82**, 174510 (2010).

[38] G. Bertaina, M. Motta, M. Rossi, E. Vitali, and D. E. Galli, Phys. Rev. Lett. **116**, 135302 (2016).

[39] M. Motta, E. Vitali, M. Rossi, D. E. Galli, and G. Bertaina, Phys. Rev. A **94**, 043627 (2016).

[40] G. Bertaina, D. E. Galli, and E. Vitali, Adv. Phys. X **2**, 302 (2017).

[41] This behavior is analog to what happens in the Lieb-Liniger model, when one decreases the coupling parameter, see J.-S. Caux and P. Calabrese, Phys. Rev. A **74**, 031605 (2006).

[42] L. Santos, G. V. Shlyapnikov, and M. Lewenstein, Phys. Rev. Lett. **90**, 250403 (2003).

[43] D. H. J. O'Dell, S. Giovanazzi, and G. Kurizki, Phys. Rev. Lett. **90**, 110402 (2003).

[44] A. Lang, C. N. Likos, M. Watzlawek, and H. Löwen, J. Phys.: Condens. Matter **12**, 5087 (2000).

[45] Conversely, density $\rho = 1/b_c \simeq 0.68$ manifests a more standard crossover from $K_L > 1$ to $K_L < 1$, not shown here, but see J. Otterbach, M. Moos, D. Muth, and M. Fleischhauer, Phys. Rev. Lett. **111**, 113001 (2013).

[46] N. D. Mermin and H. Wagner, Phys. Rev. Lett. **17**, 1133 (1966).

[47] PBC are implied.

[48] Remarkably, discrepancies of this simple expression from the calculation of the normal mode frequencies using the full dynamical matrix, as calculated in T. Neuhaus and C. N. Likos, J. Phys.: Condens. Matter **23**, 234112 (2011) are very small.

[49] C. N. Likos, B. M. Mladek, D. Gottwald, and G. Kahl, J. Chem. Phys. **126**, 224502 (2007).

[50] M. W. J. Romans, R. A. Duine, S. Sachdev, and H. T. C. Stoof, Phys. Rev. Lett. **93**, 020405 (2004).

[51] P. Pfeuty, Ann. Phys. **57**, 79 (1970).

[52] R. Coldea, D. A. Tennant, E. M. Wheeler, E. Wawrzynska, D. Prabhakaran, M. Telling, K. Habicht, P. Smeibidl, and K. Kiefer, Science **327**, 177 (2010).

[53] E. Shimshoni, G. Morigi, and S. Fishman, Phys. Rev. Lett. **106**, 010401 (2011).

[54] J. Ruhman, E. G. Dalla Torre, S. D. Huber, and E. Altman, Phys. Rev. B **85**, 125121 (2012).

[55] A. Dutta, G. Aeppli, B. K. Chakrabarti, U. Divakaran, T. F. Rosenbaum, and D. Sen, *Quantum Phase Transitions in Transverse Field Spin Models: From Statistical Physics to Quantum Information* (Cambridge University Press, Cambridge, 2015).

[56] E. Lieb, T. Schultz, and D. Mattis, Ann. Phys. **16**, 407 (1961).

[57] L. Huijse, B. Bauer, and E. Berg,

Phys. Rev. Lett. **114**, 090404 (2015).

[58] I. Affleck, Phys. Rev. Lett. **56**, 746 (1986).

[59] H. W. J. Blöte, J. L. Cardy, and M. P. Nightingale, Phys. Rev. Lett. **56**, 742 (1986).

[60] O. Alberton, J. Ruhman, E. Berg, and E. Altman, Phys. Rev. B **95**, 075132 (2017).

[61] F. D. M. Haldane, Phys. Rev. Lett. **50**, 1153 (1983).

[62] E. G. Dalla Torre, E. Berg, and E. Altman, Phys. Rev. Lett. **97**, 260401 (2006).

Supplemental Material: Quantum Critical Behavior of One-Dimensional Soft Bosons in the Continuum

We give details on the potential and relevant mean-field potentials; make some comments on the experimental realization; briefly explain the PIGS and GIFT algorithms, the optimization of the trial wavefunction, the extraction of the Luttinger parameters and of the central charge, providing also tables with the results used to produce Figs. 3 and 5 in the main text.

Note: citations in this Supplemental Material refer to the bibliography in the main paper.
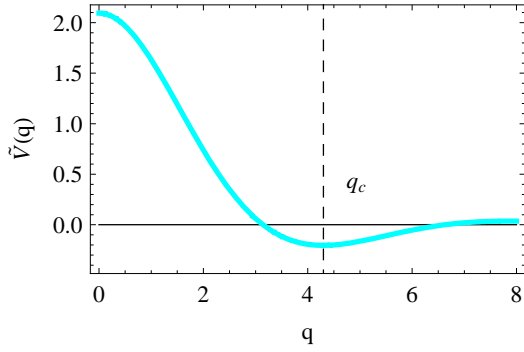
POTENTIAL AND EFFECTIVE MEAN-FIELD POTENTIAL

FIG. S1. 1D Fourier transform of the shoulder potential (with $U = 1$).

The soft-shoulder potential $V(r) = U/(1 + r^6)$ has the 1D Fourier transform (see Fig. S1)

$$\tilde{V}(q) = \int_{-\infty}^{+\infty} e^{iqr} V(r) dr =$$
$$U\pi e^{-q/2} \left[e^{-q/2} + \cos\left(\sqrt{3}q/2\right) + \sqrt{3}\sin\left(\sqrt{3}q/2\right)\right] /3 .$$
(S1)

When the density is $\rho = 2/b_c \simeq 1.37$, an approximation of the mean-field potential felt by a particle in the liquid phase can be obtained by letting all other particles on a lattice of spacing $1/\rho = b_c/2$: $V_{MF}^{LL}(r) = -V(r) + \sum_{i=-\infty}^{\infty} V(r - ib_c/2)$ (red solid line in Fig. S2). This lattice periodicity is clearly unstable, since a double well appears close to the origin: so the liquid phase is stable only thanks to kinetic energy. The mean-field potential felt by a particle in the cluster liquid phase can be approximated by letting all other particles on a lattice of spacing $2/\rho = b_c$: $V_{MF}^{CLL}(r) = -V(r) + 2\sum_{i=-\infty}^{\infty} V(r - ib_c)$, which implies that pairs of particles overlap (blue solid line in Fig. S2). Here, a clear harmonic confinement is present at
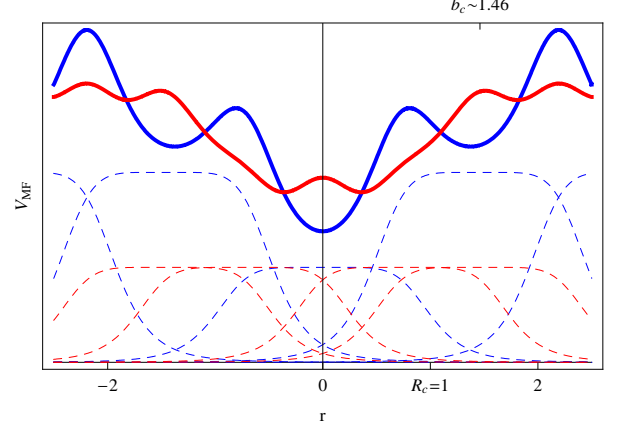

FIG. S2. Approximate mean field potentials felt by a particle in the LL phase (red solid line) and in the dimer CLL phase (blue solid line). Dashed lines indicate some of the contributions to the mean-field potential (arb. energy units).

$r = 0$, which stabilizes the cluster phase, and whose typical energy $\varepsilon_h(b_c)$ is given in the main text.

An instructive mean-field potential can also be visualized, in the LL phase, by letting three particles free, and fixing only their center of mass at the center of a lattice of the other particles with spacing $1/\rho = b_c/2$: the resulting surface, in terms of the relative distances $r_{12} = |x_1 - x_2|$ and $r_{23} = |x_2 - x_3|$, is plotted in Fig. S3. The two spheres indicate the positions of the two main equivalent minima, which clearly correspond to $(r_{12}, r_{23}) \simeq (0, b_c)$ and $(r_{12}, r_{23}) \simeq (b_c, 0)$. For particle 2, suitable orbitals centered in such minima correspond to the two states ψ_L and ψ_R introduced in the text. They define the Hilbert space governed by the Ising hamiltonian introduced in the main text.

CONSIDERATIONS ABOUT THE EXPERIMENTAL REALIZATION

In the context of ultracold Rydberg gases, the parameters of the 3D shoulder potential can be related to the Rabi frequency Ω_R and detuning Δ_R, by $U = \left(\frac{C_6 m^3 |\Delta_R|^2}{16\hbar^4}\right)^{1/3} \beta^4$ and $R_c = \left(\frac{C_6}{2\hbar|\Delta_R|}\right)^{1/6}$, where $\beta = \frac{\Omega_R}{2\Delta_R}$ is the admixture of the Rydberg level with the ground-state, and C_6 is van-der-Waals coefficient [11]. Eq.(1), in the main text, is the effective 1D Hamiltonian [21], which is relevant in an elongated quasi-1D configuration, once the transverse degrees of freedom are
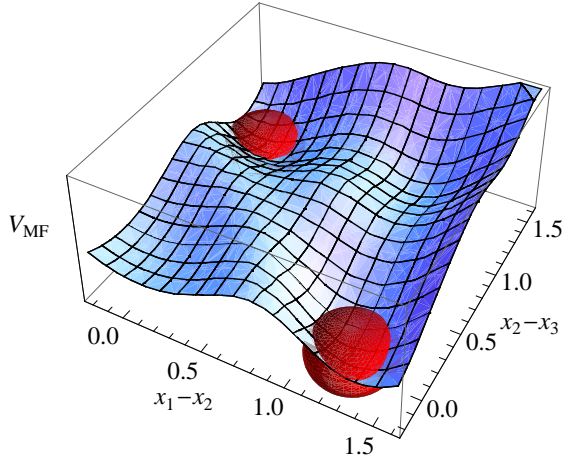
FIG. S3. Approximate mean field potential felt by three particles in the LL phase. The spheres indicate the two main minima.
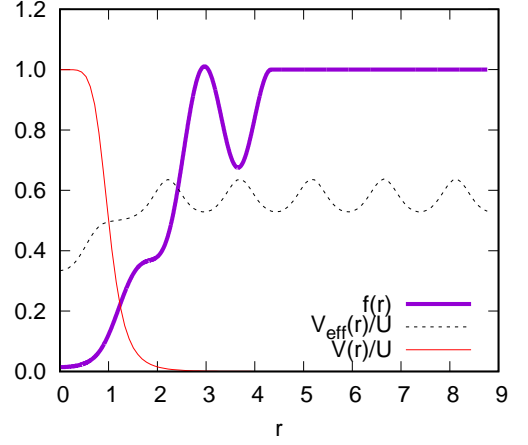

FIG. S4. Effective potential (dashed line), compared to the bare potential (solid thin line) and optimized Jastrow two-body correlation (solid thick line) at $U = 80$.

frozen in the ground state, due to strong trapping [5]. The transverse confinement size $a_\perp$ does not affect much the effective potential, if $a_\perp \lesssim R_c$. With respect to the original 3D potential, the quasi-1D interaction has reduced U and larger q_c. The condition $a_\perp \lesssim R_c$ is already under reach in current experiments, where both $a_\perp$ and R_c can be of order of 100 nm [6]. The above condition also prevents the zig-zag instability [53] for strong interactions. To experimentally probe the phase diagram in Fig.1 of the main text, one can vary detuning Δ_R, linear density n, mass m (by changing the atomic species), and $C_6 \propto \bar{n}^{11}$, by changing the addressed Rydberg level of principal number $\bar{n}$. Note that, while Rydberg levels have typical lifetimes τ_R of order of μs, Rydberg dressed atoms with small admixture β have proportionally increased lifetimes $\tau = \tau_R/\beta^2$ [16,17]. Cryogenic techniques would be beneficial to reduce the detrimental black-body radiation, due to the experimental apparatus [8]. The experimental realization of hamiltonian of Eq.(1) in the main text is presently challenging in the absence of a lattice, since no short-range hard core is enforced. However, clustering effects persist even if one introduces a hard core, provided it is small when compared to R_c.

PATH-INTEGRAL GROUND STATE METHOD

(For completeness, we add a brief description, adapted from the Supplemental Material of Ref.[38].)

The Path Integral Ground State (PIGS) Monte Carlo method is a projector technique that provides direct access to ground-state expectation values of bosonic systems, given the microscopic Hamiltonian $\hat{H}$ [34,35]. The method is exact, within unavoidable statistical error bars, which can nevertheless be reduced by performing longer simulations, as in all Monte Carlo methods. Observables $\hat{O}$ are calculated as $\langle \hat{O} \rangle = \lim_{\tau \to \infty} \langle \Psi_\tau | \hat{O} | \Psi_\tau \rangle / \langle \Psi_\tau | \Psi_\tau \rangle$, where $\Psi_\tau = e^{-\tau \hat{H}} \Psi_T$ is the imaginary-time projection of an initial trial wave-function Ψ_T. Provided non-orthogonality to the ground state, the qual-

ity of the wave-function only influences the projection time practically involved in the limit and the variance of the results.

The trial wavefunction is of the two-body Jastrow form: $\Psi_T(x_1 \ldots x_N) = \exp\left[-\frac{1}{2} \sum_{i<j} \left(u(r_{ij}) + \chi(r_{ij})\right)\right]$. The Reatto-Chester contribution

$$\chi(r) = -\alpha \log \left[\frac{\sin^2\left(\frac{\pi r}{L}\right) + \sinh^2\left(\frac{\pi \bar{R}}{L}\right)}{1 + \sinh^2\left(\frac{\pi \bar{R}}{L}\right)} \right] \quad (S2)$$

accounts for long-wavelength phonons [36,28] and allows for faster convergence of the small momenta parts of the structure factors. $\bar{R}$ is a variational parameter delimiting the long-range part from the short-range contribution. The latter is embodied in the $f(r) = \exp\left[-u(r)/2\right]$ factor, which we take as the numerical solution (described in detail in [28]) of a suitable two-body Schrödinger equation (with reduced mass $\mu = m/2$), with the effective potential

$$V_{eff}(r) = c_1 V(r) + c_2 \sum_{l=-l_C}^{l=l_C} V(r - lb), \quad (S3)$$

and the boundary condition $u(\bar{R}) = 0$. Here, the first term is a renormalized two-body potential, while the sum accounts for a series of nearby clusters in a lattice of spacing b (l=0 is excluded and $l_M = int[L/(2b)]$). All parameters in the trial wave-function are variationally optimized, as described in the next Section, before projecting with the PIGS method, in order to maximize efficiency of the simulations. One finds that typically $\bar{R} \sim 2.2$, $b \sim b_c$, and c_1 and c_2 are usually of the same order in the cluster phase. We found it is crucial to introduce such effective cluster contributions in the two-body Jastrow factor, since the variational energy per particle is typically 30% higher than the PIGS result, if one sets $c_2 = 0$. On the contrary, by properly optimizing the parameters, we obtained discrepancies of at most a few percent of the PIGS

result. A typical effective potential, and the corresponding short-range Jastrow correlation $f(r)$, are shown in Fig. S4. Notice the behavior of $f(r)$ at $r \simeq ib_c$, with $i = 1, 2$.

In the PIGS method, the imaginary time τ of propagation is split into M_P time steps of size $\delta\tau = \tau/M_P$ so that a suitable short-time approximation for the propagator can be used; in this case, we employ the fourth-order pair-Suzuki approximation [35].

The timestep is selected by performing various simulations at short fixed projection time τ with increasing number of beads M_P, and monitoring the energy per particle, looking for convergence within errorbars of order 10^{-4}. At $\rho = 1.37$, the resulting $d\tau$ approximatively follows the form $d\tau \simeq 0.1U^{-1/2}$: this is consistent with the consideration that the imaginary-time density matrix typically varies at the scale of the amplitude $l_{HCO} \propto U^{-1/4}$ of the cluster vibrational modes.

Once the timestep is selected, convergence to the ground-state is obtained by selecting a sufficiently long projection time τ, which renders the potential energy flat (within errorbars) as a function of time slice. With our optimized initial wave-functions, the typical number of time-steps for convergence is 35. Once convergence in τ is obtained, a further projection time of typically $M_F = 60$ time-slices is used to sample the intermediate scattering function $F(q, \tau)$.

Close to the transition, convergence in τ is very slow, due to the low-energy Ising mode. We have thus also employed a more refined effective potential, of the form

$$V_{eff}(r) = c_1 V(r)$$
$$+ c_2 \sum_{l=-l_C}^{l=l_C} \sum_{i=-p}^{p} V(r - lb - i\delta_l) g(i\delta_l, s_l), \quad \text{(S4)}$$

where we introduced a gaussian kernel $g(r, s_l) = \exp[-r^2/(2s_l^2)]/\mathcal{N}(s_l)$, with $\mathcal{N}(s_l) = \sum_{i=-p}^{p} \exp[-(i\delta_l)^2/(2s_l^2)]$, for better describing the clusters. The width $s_l = s_0 l^\gamma$ is allowed to increase with the cluster position, and the convolution is discretized with $p = 10$ and $\delta_l = 3s_l/p$. In the limit $s_0 \to 0$ and $\gamma \to 0$, one recovers expression (S3), while in general s_0 and γ are two additional variational parameters to be optimized.

For $U = 18$, we employed the parameters $c_1 = 1.127$, $c_2 = 1.076$, $b = 1.655$, $s_0 = 0.2$, $\alpha = 4.84$, $\bar{R} = 1.83$, and $\gamma = 0.4$. With $d\tau = 0.03$, simulations still required 100 time-slices of projection.

PARAMETERS OPTIMIZATION THROUGH SIMULATED ANNEALING

The parameters appearing in the trial wavefunction are optimized with the Variational Monte Carlo method (VMC), which corresponds to PIGS, when no imaginary-time projection is made. We employ a simulated annealing procedure in parameters' space, aiming at both reducing the energy associated to the trial wavefunction, and obtaining a good pair distribution
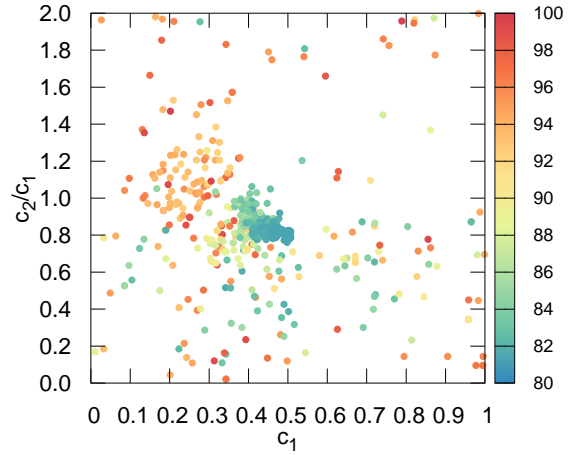

FIG. S5. Convergence of the two parameters c_1 and c_2 in a simulated annealing procedure at $U = 100$, $\rho = 1.37$. The color scale refers to the energy value of each VMC simulation.

function $g(r)$. To each configuration ξ of the parameters, the following Boltzmann weight $\lambda = \exp\left\{-\beta\left[E(\xi) + \zeta \chi^2(\xi)\right]\right\}$ is associated, with inverse temperature β, where $E(\xi)$ is the VMC energy, and

$$\chi^2(\xi) = \sum_{i}^{i_M} \frac{\left[g_0(r_i) - g_\xi(r_i)\right]^2}{\sigma_0^2(r_i) + \sigma_\xi^2(r_i)} \quad \text{(S5)}$$

is the discrepancy between the pair distribution functions obtained at a particular step g_ξ, and the one obtained with a preliminary unoptimized PIGS simulation g_0, weighted by the corresponding uncertainties σ_ξ and σ_0. This difference is evaluated only up to the i_M-th bin of the histogram of $g(r)$, which includes the first peak of $g(r)$ for $r \neq 0$. The motion of a fictitious particle is simulated in parameters' space, subjected to such Boltzmann weight, where ζ is the relative role of χ^2 with respect to E. The effective temperature is progressively decreased in order to reach the configuration having the lowest value possible of $E(\xi)$ and $\chi(\xi)$ simultaneously, and the algorithm is stopped once the variations of the weight are of the order of errorbars. The typical used value of ζ is $\sim 10^{-4}$, except close to the transition, where we observed that increasing this value led to shorter projection times in the subsequent PIGS simulations. Fig. S5 shows an example of the convergence of the two parameters c_1 and c_2.

GENETIC INVERSION VIA FALSIFICATION OF THEORIES METHOD

(For completeness, we add a brief description, adapted from the Supplemental Material of Ref.[38].)

The relation between the intermediate scattering function F, which is evaluated within the PIGS simulations, and the

dynamical structure function is

$$F(q, \tau) = \frac{1}{N} \langle e^{\tau H} \rho_q e^{-\tau H} \rho_{-q} \rangle = \int_0^\infty d\omega e^{-\tau \omega} S(q, \omega). \quad \text{(S6)}$$

This is a Fredholm equation of the first kind and is an ill-conditioned problem, because a small variation in the imaginary-time intermediate scattering function F produces a large variation in the dynamical structure factor S. At fixed momentum q, the computed values $F_j = F(q, j\delta\tau)$, where $j = 0 \ldots M$, are inherently affected by statistical uncertainties δF_j, which hinder the possibility of deterministically infer a single $S(q, \omega)$, without any other assumption on the solution. The Genetic Inversion via Falsification of Theories method (GIFT) exploits the information contained in the uncertainties to randomly generate Q compatible instances of the scattering function $F^{(z)}$, with $z = 1 \ldots Q$, which are independently analyzed to infer Q corresponding spectra $S^{(z)}$, whose *average* is taken to be the "solution". This averaging procedure, which typifies the class of stochastic search methods (See the recent review [40]), yields more accurate estimates of the spectral function than standard Maximum Entropy techniques. This method is able to resolve the first spectral peak and approximately the second one, if the errorbars of F are sufficiently small; generally speaking, the most relevant features of the spectrum are retrieved in their position and (integrated) weight.

Given an instance z, the procedure of analytic continuation from $F^{(z)}$ to $S^{(z)}$ relies on a stochastic genetic evolution of a population of spectral functions of the generic type $S^{(z)}(q, \omega) = m_0 \sum_{i=1}^{N_\omega} s_i \delta(\omega - \omega_i)$, where $m_0 = F^{(z)}(q, 0)$ and the zeroth momentum sum rule $\sum_{i=1}^{N_\omega} s_i = 1$ holds. The N_ω support frequencies ω_i are spaced linearly up to an intermediate frequency ω_m, which is of order of the maximum considered momentum squared q^2, then a logarithmic scale is used up to very high frequencies. Genetic algorithms provide an extremely efficient tool to explore a sample space by a non-local stochastic dynamics, via a survival-to-compatibility evolutionary process mimicking the natural selection rules; such evolution aims toward increasing the *fitness* of the individuals, defined as

$$\Phi^{(z)}(S) = -\sum_{j=0}^{M} \frac{1}{\delta F_j^2} \left[F_j^{(z)} - m_0 \sum_{i=1}^{N_\omega} e^{-j\delta\tau\omega_i} s_i \right]^2$$
$$- \epsilon \left[m_1 - m_0 \sum_{i=1}^{N_\omega} \omega_i s_i \right]^2, \quad \text{(S7)}$$

where the first contribution favors adherence to the data, while the second one favors the fulfillment of the f-sum rule, with $m_1 = q^2/2$ and ϵ a parameter to be tuned for efficiency. A step in the genetic evolution replaces the population of spectral functions with a new generation, by means of the "biological-like" processes of *selection*, *crossover*, *local mutation*, *non-local mutation*, which are described in detail in [37,40]. Moreover, the genetic evolution is tempered by an acceptance/rejection step based on a reference distribution
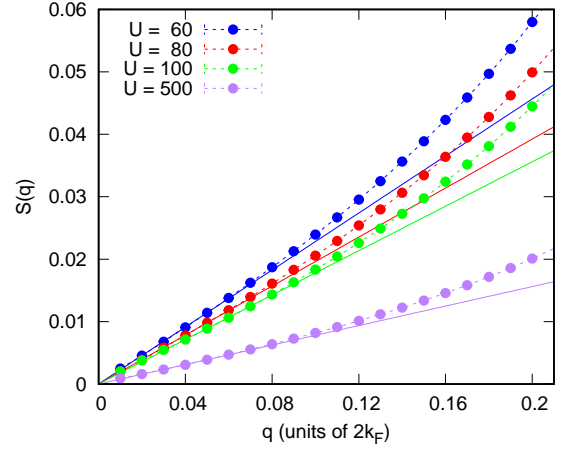

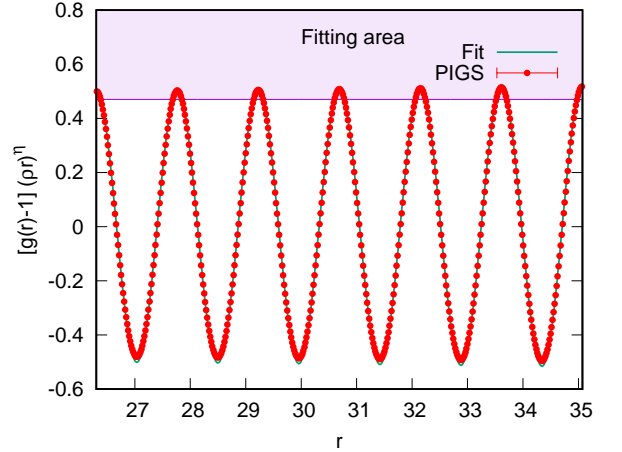FIG. S6. Low momenta behavior of $S(q)$ and corresponding linear fit, with $\rho = 1.37$.

FIG. S7. Fit of the decay of $g(r)$ for $U = 25$, $\rho = 1.37$, using Eq.(2) in the main text. The purple area highlights the fitting range.

$p^{(z)}(S) = \exp(\Phi^{(z)}(S)/T)$, where the coefficient T is used as an effective temperature in a standard simulated annealing procedure. We found that this combination is optimal in that it combines the speed of the genetic algorithm with the prevention of strong mutation-biases thanks to the simulated annealing. Convergence is reached once $|\Phi^{(z)}(S)| < 1$, and the best individual, in the sense that it does not falsify the theory represented by (S7), is chosen as the representative $S^{(z)}$. The final spectrum is obtained by taking the average over instances $\bar{S}(q, \omega) = \frac{1}{Q} \sum_{z=1}^{Q} S^{(z)}(q, \omega)$.

EXTRACTION OF THE LUTTINGER PARAMETER FROM THE STATIC STRUCTURE FACTOR

The behavior of $S(q)$ for small momenta is shown in Figure S6. Since its Luttinger liquid behavior is $S(q) \sim q K_L/(2k_F)$, we fit $2k_F S(q)/q$ with a constant. Clearly, for extremely low

U	K_L	K'_L	Δ/E_F	c
5	1.17(3)	-	0.66(11)	-
10	0.83(3)	-	0.61(14)	1.05(4)
14	-	-	-	0.98(7)
15	0.65(1)	-	0.37(7)	-
16	-	-	0.28(8)	1.06(8)
17	-	-	-	1.09(7)
18	0.52(1)	-	0.08(8)	1.3(1)
19	0.480(4)	0.163(15)	-	1.17(6)
20	0.455(5)	0.130(6)	0.46(11)	1.04(7)
21	0.430(3)	0.117(6)	-	1.03(9)
25	0.379(3)	0.100(7)	1.47(26)	1.02(4)
30	0.336(4)	0.09(2)	1.47(21)	-
40	0.281(3)	0.08(2)	-	-
60	0.23(1)	-	-	-

TABLE S1. Values of Luttinger parameters K_L and K'_L (Fig.3b in the main text), of the Ising gap Δ/E_F and the central charge c (Fig.5a in the main text), at $\rho = 1.37$.

FIG. S8. Example of the extraction of the central charge from the energy per particle $\varepsilon(N)$, for $U = 17$ (bottom) and $U = 18$ (top).

momenta, size effects become relevant, since finite imaginary-time projection has not been able to correctly reconstruct the long-distance density fluctuations, leading to a non linear behavior of the data. For this reason, the error on the fitted value of K_L has been taken to be the absolute value of the difference between the fitted K_L and the value of $2k_F S(q)/q$ for the smallest q at our disposal. The resulting K_L are summarized in Table S1.

EXTRACTION OF THE ANOMALOUS LUTTINGER PARAMETER FROM THE PAIR DISTRIBUTION FUNCTION

CLL theory implies that the long-range behavior of $g(r)$ has to be of the form of Eq.(2) in the main text. The easiest way to extract K'_L from $g(r)$ consists in evaluating the power-law exponent relative to the cosine decay. In such procedure we have neglected the $-2K_L/(2\pi\rho r)^2$ term, as well as all the cosine terms, but the first one, as their decay is usually too fast to be relevant. Values of $g(r) < 1$ are determined by short-range effects: it is thus appropriate to fit just the upper part of the peaks of $g(r)$. To make such procedure more precise, we have fitted the function $[g(r) - 1] \cdot (\rho r)^\eta$, which is supposed to behave like $\sim A_1 \cos(\pi\rho r)(\rho r)^{\eta - 2K'_L}$ for long distances, with η tuned as to have the periodic peaks at comparable heights. Thus the cosine decay is considerably softened, leading to an easier fitting of K'_L. An example of one of our fits is shown in figure S7. We have not been able to apply this methodology for $U < 18$, due to large noise-to-signal ratio, and at $U = 18$, possibly due to the role of subleading terms in the decay. The resulting K'_L are summarized in Table S1.
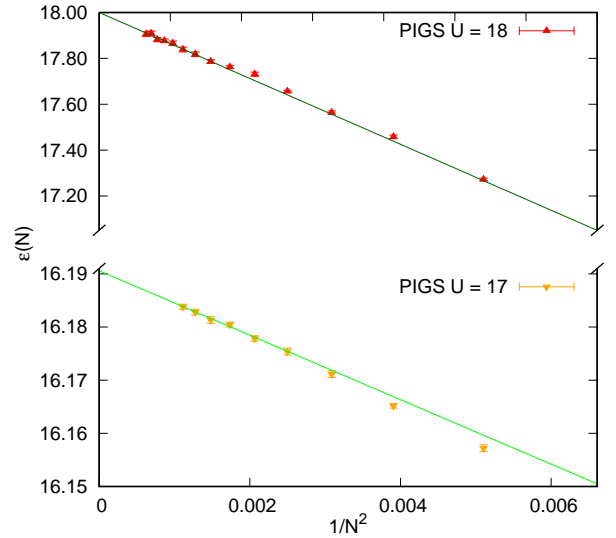
EXTRACTION OF THE CENTRAL CHARGE

We estimate the central charge c by fitting the slope of the energy per particle $\varepsilon(N) = \varepsilon_\infty - cE_F/(6K_L N^2)$ versus $1/N^2$, where K_L is inferred from Table S1. The range of considered numbers of particles is typically from $N = 10$ to $N = 40$ ($N = 100$ in some cases), and we progressively increase the minimal $N_{\min}$ used in the fit, to assess the role of higher order contributions, finding that the extracted c is generically stable if $N_{\min} = 20$. The errorbar comes from the uncertainty in $\varepsilon(N)$ and K_L, and from the variance of the extracted c at different $N_{\min} > 20$. Examples of extraction of c are shown in Fig. S8, corresponding to $U = 17$ and to the more difficult $U = 18$ point. Table S1 summarizes the results.